Research Square

Preprints are preliminary reports that have not undergone peer review.
They should not be considered conclusive, used to inform clinical practice,
or referenced by the media as validated information.

Mechanical characterization and constitutive modelling of 8011-O aluminium alloy sheets for fin forming

Ping Li
Hefei University of Technology
Lin Zhong
Hefei University of Technology
Xu Cheng
Hefei University of Technology
Yingsheng Li
Hefei University of Technology
Yang Wang
Hefei University of Technology
Baisong Liu
Hefei University of Technology
Mengchen Zhu
Hefei University of Technology
Kemin Xue
xuekm@hfut.edu.cn

Hefei University of Technology

Research Article

Keywords: 8011-O aluminium alloy, yield criteria, constitutive model, Stamping forming

Posted Date: November 20th, 2026

DOI: https://doi.org/10.21203/rs.3.rs-11633989/v1

License: This work is licensed under a Creative Commons Attribution 4.0 International License.
Read Full License

Additional Declarations: No competing interests reported.

Mechanical characterization and constitutive modelling of 8011-O aluminium alloy sheets for fin forming

Abstract

Accurate representation of anisotropy, strain rate sensitivity and fracture is needed to simulate the forming of thin aluminium fins. This study characterizes 8011-O aluminium alloy sheets with a thickness of 0.3 mm and develops material descriptions for fin forming. Room-temperature uniaxial tensile tests were conducted along seven in-plane orientations, and tests in the rolling direction covered strain rates from 10^{-4} to 10^{3} s^{-1}. Shear and notched tensile tests were used to characterize fracture under different stress states. The measurements showed pronounced directional variation in yield stress and plastic strain ratio, together with an increase in flow stress with strain rate. A modified Hill48 formulation was fitted to the directional yield stresses and plastic strain ratios, and a Johnson-Cook constitutive model with a polynomial strain rate coefficient was introduced. A Johnson-Cook fracture model was calibrated using the fracture tests. These material descriptions were then used in finite element simulations of fin piercing and flanging. The simulations identified localized thinning near the punch radius. Comparison with forming experiments gave a maximum relative error of 9.68% in the thinning ratio. Both the simulations and experiments showed fracture at a punch speed of 500 mm s^{-1}. The results provide a basis for assessing thickness variation and fracture during 8011-O aluminium fin forming.

Key words: 8011-O aluminium alloy, yield criteria, constitutive model, Stamping forming

1.Introduction

Thin aluminium fins are manufactured through successive forming operations in which local thinning and fracture can limit the attainable geometry. Numerical studies of related plate-fin structures have examined manufacturing-induced deformation and residual stress [1]. Research on aluminium sheet drawing and joints for plate-fin heat exchangers has also addressed the relationship between processing, microstructure and mechanical performance [2, 3]. For the 8011-O fins considered here, predicting the response during piercing and flanging requires a material description that accounts for plastic anisotropy, strain-rate dependence and fracture.

Material models link mechanical measurements to the prediction of forming defects. Studies of sheet forming and related lightweight structures have used damage models, anisotropic flow rules and numerical analysis to describe deformation and defect formation [4–6]. Extensions of anisotropic yield criteria and investigations of electrically assisted dynamic deformation illustrate the different material responses considered in sheet-metal processing [7, 8]. Processing history is another relevant factor: annealing after cryogenic rolling has been investigated for 8011 aluminium

alloy, while cryogenic treatment has been studied for 3102 aluminium alloy [9, 10]. These findings establish the importance of the material condition and loading environment when selecting data for a forming simulation.

Plastic anisotropy affects both the onset of yielding and the distribution of plastic strain in a rolled sheet. Changes in anisotropic plasticity and fracture with natural ageing have been reported for 7075 aluminium alloy [11]. The conventional Hill48 yield criterion provides a compact description of directional behaviour, but its ability to reproduce directional yield stresses and plastic strain ratios simultaneously is limited; modified formulations have been developed to address this issue [12]. More detailed descriptions of anisotropic hardening and anisotropic ductile fracture have also been investigated [13, 14]. For the present fin-forming application, the directional yield stresses and plastic strain ratios are therefore both used in the calibration and assessment of the yield formulation.

Changes in forming speed introduce a further requirement for the constitutive description. Studies of 7A75 aluminium alloy over a wide range of strain rates and of 6061 aluminium alloy under hot rolling conditions illustrate the need to calibrate flow behaviour over the relevant deformation range [15, 16]. Rate-dependent constitutive modelling has also been investigated for 7A04-T6 aluminium alloy [17]. For 6061 aluminium alloy, a modified Johnson-Cook formulation incorporates Voce hardening and adjustments to the strain-rate and thermal terms [18]. For 6016-T6 aluminium alloy sheets, integration of the strain-rate hardening coefficient has been used to modify the Johnson-Cook model [19]. These approaches provide a basis for selecting a constitutive formulation, while the rate dependence of the 8011-O sheet used here must be established from its own tensile measurements.

Fracture prediction requires additional information about the loading mode and stress state. Johnson-Cook damage parameters have been determined for laminated 7xxx aluminium alloy and used in numerical simulations [20]. Further studies have assessed uncoupled damage models in incremental sheet forming [21], coupled damage and viscoplasticity at elevated temperatures [22], and damage evolution in rivet-bonded joints [23]. These applications emphasise the need to calibrate fracture behaviour for loading conditions relevant to the intended process. In thin-fin forming, the stress states near a piercing edge or a flanging radius cannot be represented by a single uniaxial tensile test. Shear and notched tensile tests are therefore included in the present characterisation.

The present study combines mechanical characterisation and finite element simulation for 0.3 mm thick 8011-O aluminium alloy sheets used in fin forming. Room-temperature tensile tests are performed along seven in-plane orientations, and tests in the rolling direction cover strain rates from 10^{-4} to 10^{3} s^{-1}. Shear and notched tensile tests provide additional data for fracture calibration. A

direction-dependent Hill48 formulation and a Johnson-Cook constitutive model with a rate-dependent coefficient are calibrated from the measurements, together with a Johnson-Cook fracture model. These material descriptions are then applied to simulations of fin piercing and flanging and assessed against forming experiments. The objective is to evaluate their ability to describe thickness variation and fracture occurrence under the investigated forming conditions.

2 Materials and methods

2.1 Specimen preparation

The experimental material is 8011 aluminium alloy for air conditioning fins, with a thickness of 0.3 mm, and its chemical composition is shown in Table 1. The dimensions of the specimen are shown in Fig. 1(a). Specimens were cut by wire electrical discharge machining at angles of 0°, 15°, 30°, 45°, 60°, 75°, and 90° to the rolling direction, as shown in Fig. 1(b). The edges of the sample were polished with 800# and 400# sandpaper. The uniaxial tensile specimen geometry was designed with reference to ISO 26203-2:2011 (Metallic materials — Tensile testing at high strain rates — Part 2: Servo-hydraulic and other test systems). The four shear and notched specimen geometries were adapted from Chang et al. [20]. Representative tensile specimens after testing are shown in Fig. 2.

Table 1 Chemical composition of the 8011 aluminium alloy(wt-%)

Element	Si	Fe	Cu	Mn	Mg	Cr	Zn	Al
Content	0.5-0.9	0.6-1.0	<0.1	0.2	<0.05	0.05	0.1	Bal

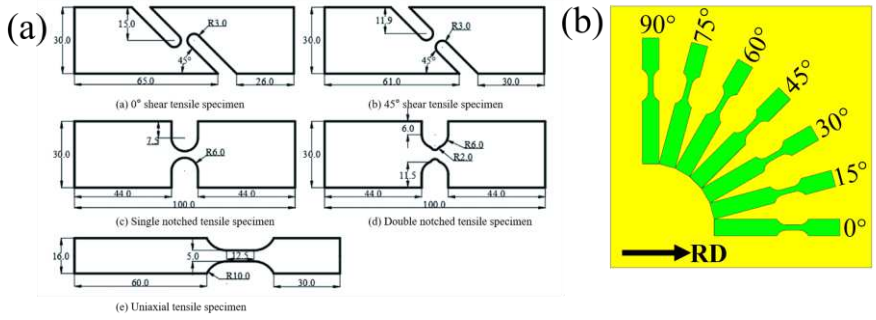


Fig. 1 Uniaxial tensile specimen of 8011 aluminium alloy: a) Specimen dimensions; b) Machining directions.

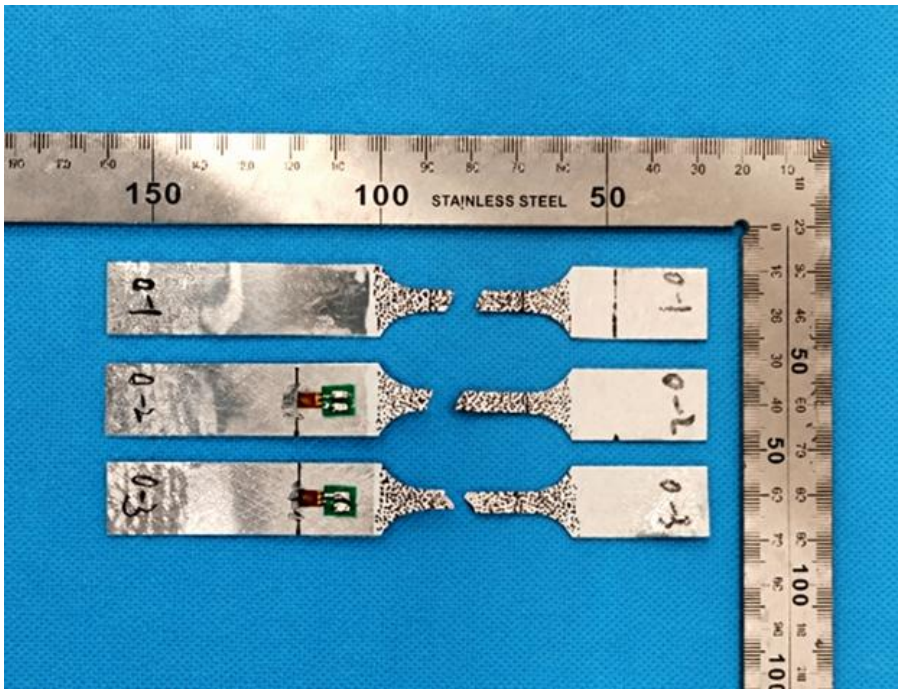


Fig. 2 Representative 8011 aluminium alloy tensile specimens after testing.

2.2 Experimental procedures

To determine the Hill48 yield criteria and the Johnson-Cook constitutive model of 8011 aluminium alloy, quasi-static tensile tests were performed at room temperature with various orientations. In addition, dynamic tensile tests were performed at room temperature in the rolling direction. The quasi-static tensile tests were performed using a WDW-10E machine manufactured by Jinan Liantai Testing Machine Co., LTD. in China. Dynamic tensile testing were conducted using a VHS 160/100-20 machine manufactured by Instron Test Equipment Trading Co., Ltd. in Shanghai. For the quasi-static tensile testing, the collet was adjusted to stretch the specimens at 0.075 mm/min and 7.5 mm/min (strain rates of 10^{-4} s^{-1} and 10^{-2} s^{-1}). In the dynamic tensile test, the loading speed of the collet was set to 750 mm/min, 75,000 mm/min, and 750,000 mm/min (strain rates 1 s^{-1}, 10^{2} s^{-1}, and 10^{3} s^{-1}) to obtain the plastic flow behaviour and damage evolution of 8011 aluminium alloy under different strain rate. An extensometer was used during tensile testing.

In order to determine the parameters of the Johnson-Cook damage fracture model, fracture property tests (0° shear and 45° shear tensile tests, single-notch and double-notch tensile tests, and uniaxial tensile tests) were conducted at room temperature. All tensile specimens were stretched by strain rate of 10^{-2} s^{-1}, and the loading speeds corresponding to each specimen in Fig. 1(a) (a, b, c, d) were 2 mm/min, 2 mm/min, 3.6 mm/min and 3.6 mm/min, respectively. The above tests were repeated three times under the same strain rate in order to ensure the accuracy of the measured data.

3 Results

3.1 Hill48 yield criteria

3.1.1 Original Hill48 yield model

The original Hill48 yield criterion can be expressed as follows[24]:

$$2\Phi(\sigma_{ij}) = f(\sigma_y - \sigma_z)^2 + g(\sigma_z - \sigma_x)^2 + h(\sigma_x - \sigma_y)^2 + 2l\tau_{yz}^2 + 2m\tau_{zx}^2 + 2n\tau_{xy}^2 = 1 \quad (1)$$

Where, Φ is the yield function; σ_{ij} is the stress component; σ_x, σ_y, and σ_z are the normal stress components in the x, y, and z directions, respectively; τ_{xy}, τ_{yz}, and τ_{zx} are the shear stress components in the xy, yz, and zx planes, respectively; and f, g, h, n ,l and m are the anisotropy parameters.

In the plane stress state can be expressed as:

$$2\Phi(\sigma_{ij}) = (g+h)\sigma_x^2 - 2h\sigma_x\sigma_y + (f+h)\sigma_y^2 + 2n\tau_{xy}^2 = 1 \quad (2)$$

In the case of a uniaxial tensile specimen at an angle α to the rolling direction, the stress components can be expressed as follows:

$$\begin{aligned} \sigma_x &= \sigma_\alpha \cos^2\alpha \\ \sigma_y &= \sigma_\alpha \sin^2\alpha \\ \tau_{xy} &= \sigma_\alpha \sin\alpha\cos\alpha \end{aligned} \quad (3)$$

The substitution of Eq. (3) into Eq. (2) results in the calculation of the uniaxial tensile yield stress, denoted by σ_α.

$$\sigma_\alpha = \frac{1}{\sqrt{f\sin^2\alpha + g\cos^2\alpha + h + (2n - f - g - 4h)\sin^2\alpha\cos^2\alpha}} \quad (4)$$

As demonstrated in Eq. (4), the uniaxial tensile stresses with respect to 0°, 45°, and 90° along the rolling direction (RD) are as follows:

$$\begin{aligned} \sigma_0 &= \frac{1}{\sqrt{g+h}} \\ \sigma_{45} &= \frac{2}{\sqrt{f+g+2n}} \\ \sigma_{90} &= \frac{1}{\sqrt{f+h}} \end{aligned} \quad (5)$$

The following equation is derived from Eq. (5):

$$\begin{aligned} g &= \frac{1}{\sigma_0^2} - h \\ f &= \frac{1}{\sigma_{90}^2} - h \\ 2n &= \frac{4}{\sigma_{45}^2} - f - g \end{aligned} \quad (6)$$

Substitution of Eq. (6) into Eq. (4) results in,

$$\sigma_\alpha = \frac{1}{\sqrt{\frac{\sin^2\alpha}{\sigma_{90}^2}+\frac{\cos^2\alpha}{\sigma_0^2}+(\frac{4}{\sigma_{45}^2}-\frac{2}{\sigma_0^2}-\frac{2}{\sigma_{90}^2})\sin^2\alpha\cos^2\alpha}} \tag{7}$$

Eq. (7) demonstrates that if the anisotropy parameter satisfies Eq. (6), the uniaxial tensile yield stress in any direction may be uniquely identified by σ_0, σ_{45}, and σ_{90}. It is also clear that the value of h does not affect the uniaxial tensile stress prediction.

In accordance with the Drucker flow criterion[25], the anisotropy parameter r_α for uniaxial stretching along the α direction can be expressed as follows:

$$r_\alpha = \frac{h+(2n-f-g-4h)\sin^2\alpha\cos^2\alpha}{f\sin^2\alpha+g\cos^2\alpha} \tag{8}$$

Similarly, according to Eq. (8),there:

$$\begin{aligned} r_0 &= \frac{h}{g} \\ r_{45} &= \frac{2n-f-g}{2(f+g)} \\ r_{90} &= \frac{h}{f} \end{aligned} \tag{9}$$

The anisotropy parameter is determined from Eq. (9), as follows:

$$\begin{aligned} g &= \frac{h}{r_0} \\ f &= \frac{h}{r_{90}} \\ 2n &= (2r_{45}+1)(f+g) \end{aligned} \tag{10}$$

The substitution of Eq. (10) into Eq. (8) results in the following expression for r_α with respect to r_0, r_{45} and r_{90}:

$$r_\alpha = \frac{1+[2r_{45}(\frac{1}{r_0}+\frac{1}{r_{90}})-4]\sin^2\alpha\cos^2\alpha}{\frac{\sin^2\alpha}{r_{90}}+\frac{\cos^2\alpha}{r_0}} \tag{11}$$

Eq. (11) shows that if the anisotropy parameter satisfies Eq. (10), the unidirectional stretch r_α in any direction may be uniquely predicted by r_0, r_{45}, and r_{90}. Existing Hill48 anisotropy parameter formulations[26] based on non-associative flow laws fulfil Eq. (6) and (10), respectively. However, it is crucial to note that the actual uniaxial tensile yield stress of material and *r*-value may not follow these correlations. The Hill48 yield criterion can only predict the uniaxial tensile yield stress and *r*-value in any direction if Eq. (7) and (11) are roughly met. As a result, even when using the non-associative flow laws, the ability to improve forecast accuracy is limited. A key reason for the

inability of the Hill48 yield criterion to accurately describe both the yield stress and the *r*-value is that it contains only four anisotropic parameters in the plane stress state. This limits the ability of the model to describe the complex anisotropic behaviour of the material. It would enhance the characterisation ability of the model by introducing additional parameters without changing the structure of the original quadratic yield function. These additional parameters are able to capture the anisotropic properties of the sheet more comprehensively, which is expected to significantly improve the accuracy of the model in predicting the uniaxial tensile yield stress and anisotropic *r*-values.

3.1.2 Modified Hill48 yield model

When constructing the orthogonal anisotropic yield equation, the relative relationship between the reference coordinate system and the anisotropic principal axis needs to be clarified. The yield function constructed based on the stress component of the reference coordinate system needs to be transformed to the principal axis coordinate system by the stress tensor to obtain the yield trajectory equation. Obviously, the yield trajectory equation should cover the angle between the stress principal axis and the reference coordinate system. In particular, the yield function based on the principal stress components in the stress principal axis coordinate system is the yield trajectory function. Therefore, the stress principal axis orientation is a central variable in elucidating the yielding behaviour of orthotropic anisotropic plates. In the plane stress state, the stress principal axis direction varies only in the plane and is consistent with the loading direction of the specimen in the uniaxial tensile test. Based on this, there is a clear theoretical basis for refining the anisotropy parameter as a function of the stress principal axis direction. By correlating the anisotropy parameter with the stress principal axis direction, the yield behaviour of the material under different loading paths can be described more accurately and the predictive ability of the model can be improved.

The modified Hill48 yield criterion remains consistent with the original equation formulation.

$$2\Phi(\sigma_{ij}) = (G+H)\sigma_x^2 - 2H\sigma_x\sigma_y + (F+H)\sigma_y^2 + 2N\tau_{xy}^2 = 1 \tag{12}$$

Where, the variables *F*, *G*, *H*, and *N* are redefined as a function of the direction of the stress principal axis. The construction of the modified Hill48 model is outlined as follows.

Substituting Eq. (6) into Eq. (8), there is,

$$r_\alpha = \frac{h+(\frac{4}{\sigma_{45}^2}-\frac{2}{\sigma_{90}^2}-\frac{2}{\sigma_0^2})\sin^2\alpha\cos^2\alpha}{(\frac{1}{\sigma_{90}^2}-h)\sin^2\alpha+(\frac{1}{\sigma_0^2}-h)\cos^2\alpha} \tag{13}$$

From Eq. (13), there is a direct correlation between the uniaxial tensile *r*-value and the anisotropic parameter *h* in different directions when the anisotropic parameter meets the conditions of Eq. (6). If the anisotropic properties of the material fully conform to the prediction range of the

Hill48 model, the *r*-values in different directions can be accurately predicted by Eq. (13). However, this situation is more difficult to realise in practice. Therefore, *h* is reset to a variable parameter for mapping the variation of *r*-values in different directions. According to Eq. (13) can be obtained:

$$h(\alpha)=\frac{(\frac{\sin^2\alpha}{\sigma_{90}^2}+\frac{\cos^2\alpha}{\sigma_0^2})r_\alpha^{\exp}-(\frac{4}{\sigma_{45}^2}-\frac{2}{\sigma_{90}^2}-\frac{2}{\sigma_0^2})\sin^2\alpha\cos^2\alpha}{1+r_\alpha^{\exp}} \tag{14}$$

Where, $r_\alpha^{\exp}$ is the experimental r-value in direction α, and $h(\alpha)$ is the anisotropy parameter calculated from the directional r-values.

According to Eq. (6) and (7), the predicted uniaxial tensile yield stress is as follows:

$$\sigma_\alpha^{\text{pre}}=\frac{1}{\sqrt{\frac{\sin^2\alpha}{\sigma_{90}^2}+\frac{\cos^2\alpha}{\sigma_0^2}+(\frac{4}{\sigma_{45}^2}-\frac{2}{\sigma_0^2}-\frac{2}{\sigma_{90}^2})\sin^2\alpha\cos^2\alpha}} \tag{15}$$

From Eq. (15), it can be seen that the predicted values of uniaxial tensile yield stresses are equal to the experimental values only in the three directions of 0°, 45° and 90°, while there are prediction errors in all other directions. Therefore, the correction coefficient W_α corresponding to the uniaxially loaded stress state is introduced for correcting the uniaxially loaded stress prediction results.

$$W_\alpha=\frac{\sigma_\alpha^{\text{pre}}}{\sigma_\alpha^{\exp}} \tag{16}$$

Where, $\sigma_\alpha^{\exp}$ is the uniaxial loading test yield stress in a specific direction α.

Substituting Eq. (15) into Eq. (16) yields:

$$W_\alpha=\frac{1}{\sigma_\alpha^{\exp}\sqrt{f\sin^2\alpha+g\cos^2\alpha+h+(2n-f-g-4h)\sin^2\alpha\cos^2\alpha}} \tag{17}$$

The modified uniaxially loaded yield stress $\sigma_\alpha^{\text{m-pre}}$ can be expressed as:

$$\sigma_\alpha^{\text{m}-\text{pre}}=\frac{1}{W_\alpha\sqrt{f\sin^2\alpha+g\cos^2\alpha+h+(2n-f-g-4h)\sin^2\alpha\cos^2\alpha}} \tag{18}$$

The anisotropy parameter is redefined by introducing correction coefficients into the original anisotropy parameter:

$$\begin{aligned}H_\alpha&=W_\alpha^2h\\G_\alpha&=W_\alpha^2g\\F_\alpha&=W_\alpha^2f\\N_\alpha&=W_\alpha^2n\end{aligned} \tag{19}$$

Substituting Eq. (6) into Eq. (19),

$$
\begin{aligned}
H_\alpha &= W_\alpha^2 h(\alpha) \\
G_\alpha &= W_\alpha^2 (\frac{1}{\sigma_0^2} - h(\alpha)) \\
F_\alpha &= W_\alpha^2 (\frac{1}{\sigma_{90}^2} - h(\alpha)) \\
N_\alpha &= \frac{W_\alpha^2}{2} (\frac{4}{\sigma_{45}^2} - f - g)
\end{aligned}
\tag{20}
$$

3.1.3 Parameter determination of the modified Hill48 yield criterion

The uniaxial tensile stress-strain curves of 8011-O aluminium alloy in different orientations (0°, 15°, 30°, 45°, 60°, 75°, 90°) at a strain rate of $10^{-2}s^{-1}$ are shown in Fig. 3, and the anisotropic *r*-values and yield stress are shown in Table 2.

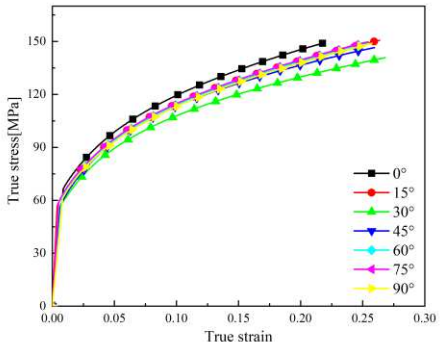


Fig. 3 Stress-strain curves of 8011 aluminum alloy in different directions

Table 2 Experimental *r*-value and yield stress

Direction	0°	15°	30°	45°	60°	75°	90°
r-value	0.4035	0.5901	1.2053	1.7860	1.1960	0.6144	0.4571
Yield stress(MPa)	66.5360	56.3436	56.6228	60.9195	65.2471	59.1462	60.9554

The procedure for determining the anisotropy parameter is outlined as follows:

(1) Fitting uniaxial tensile yield stress and *r*-value with α-angle as polynomial functions, respectively:

$$
\begin{aligned}
\sigma_\alpha^{\exp} &= I_0 + I_1\alpha + I_2\alpha^2 + I_3\alpha^3 + I_4\alpha^4 + I_5\alpha^5 (0^\circ \le \alpha \le 90^\circ) \\
r_\alpha^{\exp} &= J_0 + J_1\alpha + J_2\alpha^2 + J_3\alpha^3 + J_4\alpha^4 + J_5\alpha^5 (0^\circ \le \alpha \le 90^\circ)
\end{aligned}
\tag{21}
$$

Where, $\sigma_\alpha^{\exp}$ and $r_\alpha^{\exp}$ are the uniaxial tensile stress and uniaxial tensile *r* values in different directions, respectively; I_i and J_i (i=0 to 5) are the fitting coefficients.

(2) Solve for $h(\alpha)$ by substituting $r_\alpha^{\exp}$ into equation (14).

(3) Solve for the correction factor W_α by substituting $\sigma_\alpha^{\exp}$ into Eq. (17).

(4) The anisotropy parameter is ascertained by substituting $h(\alpha)$ and $W\alpha$ into Eq. (20).

The Hill48-S and Hill48-r models give poor predictions in directions other than 0°, 45°, and 90° because they only use uniaxial tensile yield stress and *r*-values in these three directions when determining the anisotropy parameter.The modified Hill48 model is able to accurately predict both the uniaxial tensile yield stress and the r value simultaneously and can reflect the change of the yield

stress and the *r*-value with angle as shown in Figures 4 (a) and (b).

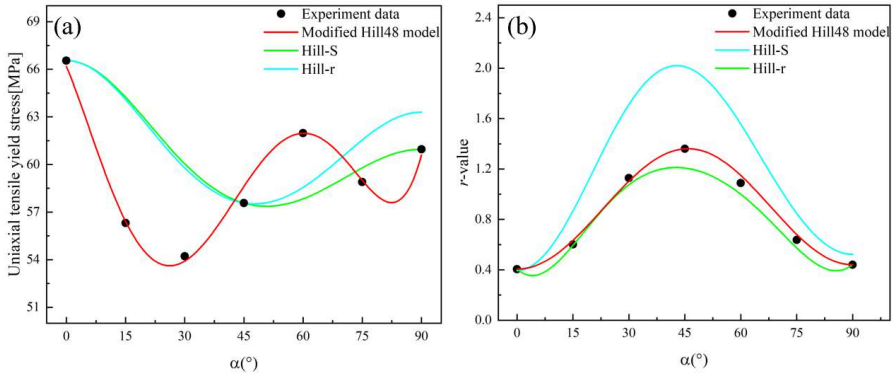


Fig. 4 Comparison of uniaxial tensile yield stress and r-value predicted by different models with experimental results: (a) yield stress; (b) r-value.

3.2 Johnson-Cook constitutive model

The phenomenologically based Johnson-Cook model has few parameters and a simple expression form, which can be used to describe the dynamic and quasi-static deformation behaviour of materials over a large range of strain rates. Currently widely used in finite element software, the general expression of the J-C model is as follows[27]:

$$\sigma = (A_1 + A_2\varepsilon^{A_3})(1 + A_4 \ln\dot{\varepsilon}^*)[1 - (T^*)^{A_5}] \tag{22}$$

Where, σ is the equivalent stress and ε is the equivalent strain. The normalized strain rate is $\dot{\varepsilon}^* = \dot{\varepsilon}/\dot{\varepsilon}_0$, where $\dot{\varepsilon}$ is the experimental strain rate and $\dot{\varepsilon}_0 = 10^{-4}s^{-1}$ is the reference strain rate. The normalized temperature is $T^* = (T - T_r)/(T_{\text{melt}} - T_r)$, where T is the experimental temperature, T_r is room temperature, and T_{melt} is the melting temperature. The parameters A_1, A_2, A_3, A_4, and A_5 are determined by fitting the experimental data.

The quasi-static and dynamic tensile test data for 8011 aluminium alloy are shown in Fig. 5. The material parameters of the Johnson-Cook constitutive model were determined as follows:

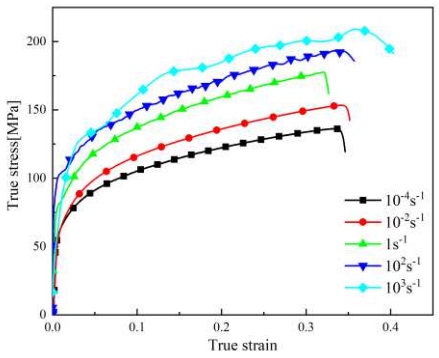


Fig. 5 Mechanical curves of 8011-O aluminum alloy at different strain rates

(1) The parameters A_1, A_2 and A_3 in the Johnson-Cook constitutive model for 8011 aluminium alloy characterize the material's work-hardening behavior. When a uniaxial tensile specimen is subjected to quasi-static stretching at room temperature with a deformation rate of 0.075 mm/min, where T=T_r and $\dot{\varepsilon}_0$=$10^{-4}s^{-1}$. Eq. (22) may be simplified as:

$$\sigma = A_1 + A_2\varepsilon^{A_3} \tag{23}$$

The taking of the logarithm of Eq. (23) results in the following:

$$\ln(\sigma - A_1) = \ln A_2 + A_3 \ln\varepsilon \tag{24}$$

A_1 is the yield stress at the reference strain rate, which is determined to be 59.6 MPa. In order to determine the material constants A_2 and A_3, the stress-strain data at the reference strain rate is plotted in Fig. 6. The value of A_3 can be determined by fitting the slope of the data points. The intercept on the vertical axis is equal to ln A2. The values of A_2 and A_3 can be determined as 163.78 and 0.59211, respectively.

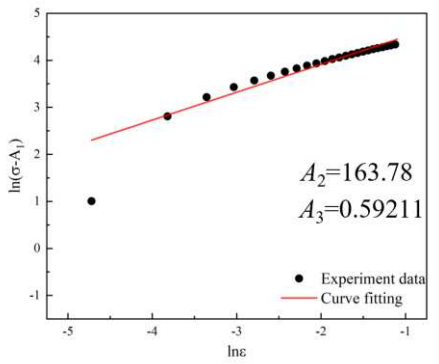


Fig. 6 The relationship between lnε and ln(σ-A_1)

(2) In the original Johnson-Cook constitutive model, stress is generally assumed to be linearly related to log strain rate. However, this simplifying assumption does not take into account the nonlinear strain rate sensitivity that is actually observed in the stress-strain relationship, resulting in significant prediction errors. In order to address this problem, the strain rate sensitivity parameter

A_4 in the original Johnson-Cook constitutive model was refined to a polynomial function of strain rate. The function was determined by selecting test data corresponding to strains of 0.1, 0.15, 0.2, and 0.25 at different strain rates. The resulting data were then plotted on a coordinate plane, with $ln\dot{\varepsilon}$ on the horizontal axis and $[\sigma(\varepsilon,\dot{\varepsilon})/\sigma(\varepsilon)\text{-}1]/\ln(\dot{\varepsilon}/\varepsilon_0)$ on the vertical axis, as illustrated in Fig. 7. The data points were then fitted with a polynomial, as demonstrated in Eq. (25). Here, $x = \ln[\dot{\varepsilon}/(1s^{-1})]$ is the dimensionless logarithmic strain-rate variable used in Eqs. (25)–(27); this definition preserves the fitted coefficients obtained with strain rates expressed in s^{-1}.

$$A_4(x) = q_0 + q_1 x + q_2 x^2 + q_3 x^3 \tag{25}$$

The original Johnson-Cook model can be modified to:

$$\sigma(\varepsilon, \dot{\varepsilon}) = (A_1 + A_2 \varepsilon^{A_3})[1 + A_4(x)\ln\dot{\varepsilon}^*] \tag{26}$$

The coefficients in Eq. (25) were obtained by fitting the data points in Fig. 7 at different strains. The fitting results are shown in Table 3, and the coefficients were determined by calculating the average of the four fitting results.

Table 3 Values of the coefficients in the MJ-C model.

True Strain	A_4 Fitting parameter			
	q_0	q_1	q_2	q_3
0.1	0.03839	-3.392×10^{-4}	-2.314×10^{-4}	-3.602×10^{-5}
0.15	0.03566	-8.259×10^{-4}	-2.858×10^{-4}	-5.902×10^{-5}
0.2	0.03252	-8.359×10^{-4}	-3.255×10^{-4}	-6.109×10^{-5}
0.25	0.02998	-1.701×10^{-5}	-3.075×10^{-4}	-4.447×10^{-5}
AverageValue	0.03414	-5.045×10^{-4}	-2.875×10^{-4}	-5.015×10^{-5}

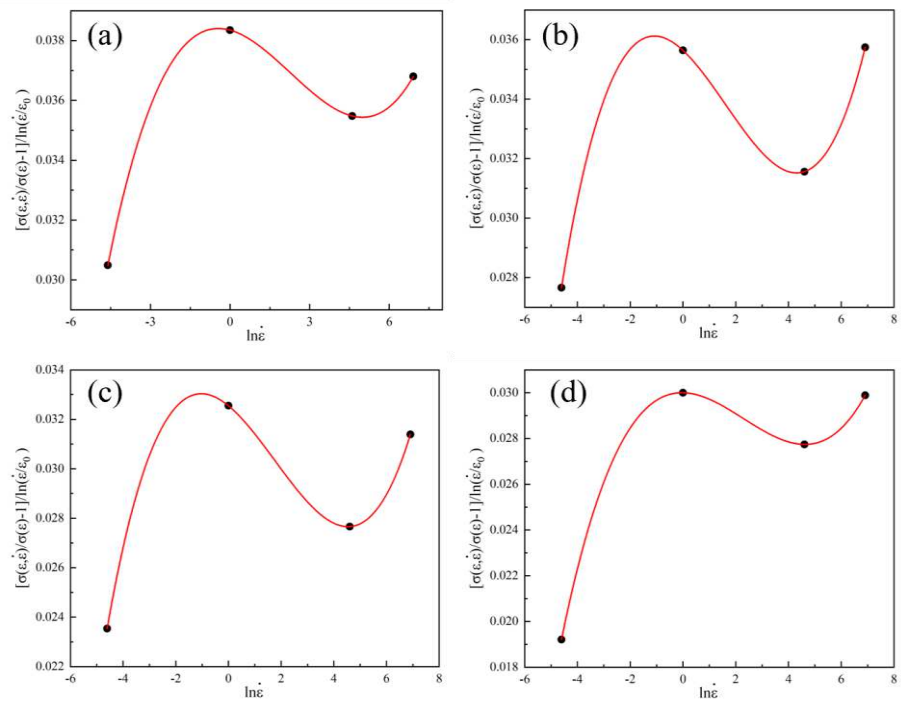


Fig. 7 Relationship between $[\sigma(\varepsilon,\dot{\varepsilon})/\sigma(\varepsilon)\text{-}1]/\ln(\dot{\varepsilon}/\varepsilon_0)$ and $\ln\dot{\varepsilon}$: (a) strain 0.1; (b) strain 0.15; (c) strain 0.2; (d) strain 0.25

The MJ-C model can be expressed as follows:

$$\sigma = (59.6 + 163.78\varepsilon^{0.59211})[1 + A_4(x)\ln\dot{\varepsilon}^*]$$
$$A_4(x) = 0.03414 - 5.045 \times 10^{-4}x - 2.875 \times 10^{-4}x^2 - 5.015 \times 10^{-5}x^3 \quad (27)$$

In order to assess the accuracy of the MJ-C model, the stress-strain data during the plastic deformation stage were compared with the predicted data from the MJ-C model as shown in Fig. 8. The fitting accuracy of the constitutive model was assessed using the calculation of the correlation coefficient R and the average relative error (*AARE*), as shown in Eq. (28) and Eq. (29).

$$R = \frac{\sum_{i=1}^{N}(L_i-\overline{L})(M_i-\overline{M})}{\sqrt{[\sum_{i=1}^{N}(L_i-\overline{L})^2][\sum_{i=1}^{N}(M_i-\overline{M})^2]}} \quad (28)$$

$$\mathrm{AARE} = \frac{100\%}{N}\sum_{i=1}^{N}\left|\frac{L_i-M_i}{L_i}\right| \quad (29)$$

Where N is the number of samples, L_i and M_i are the experimental and predicted values of the true stress, respectively; $\bar{L}$ and $\bar{M}$ are the mean values of the experimental true stress and predicted true stress, respectively.

A comparison of the experimental data with the predicted results of the MJ-C constitutive model is given in Fig. 8. The results show that the MJ-C model can effectively describe the stress-

strain behaviour of 8011-O aluminium alloy during the plastic deformation stage. The *R* and *AARE* values of the MJ-C model are given in Table 4. After the modification, the maximum *AARE* for the predicted data is only 4.0213%. These findings indicate that the MJ-C model can accurately predict the plastic flow behaviour.

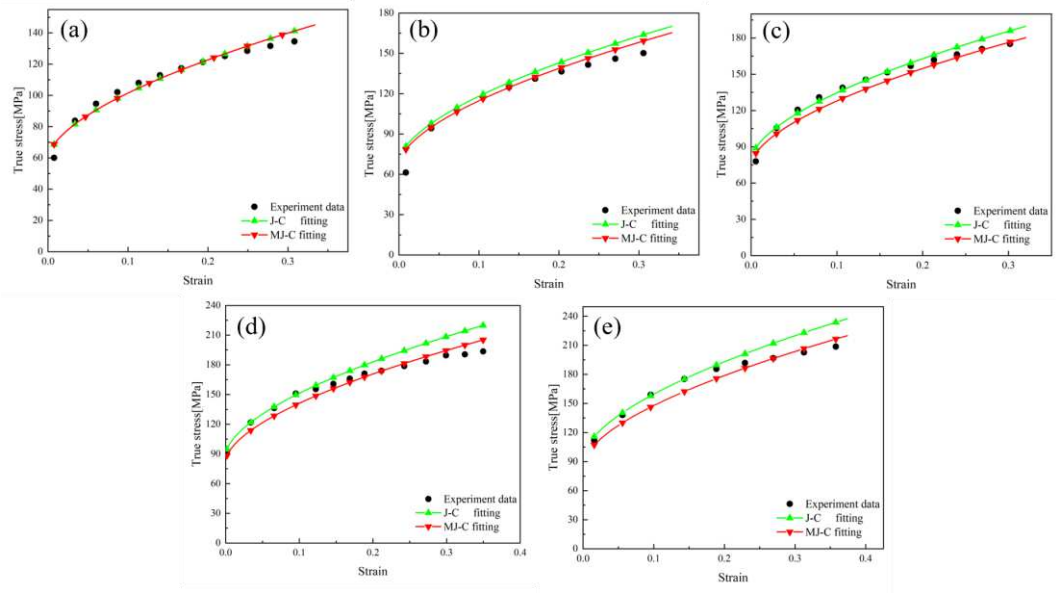


Fig. 8 Comparison of experimental and predicted data with MJ-C model: (a) $10^{-4}s^{-1}$; (b) $10^{-2}s^{-1}$; (c) $1s^{-1}$; (d) $10^{2}s^{-1}$; (e) $10^{3}s^{-1}$.

Table 4 The *R* value and *AARE* value of MJ-C

Strain Rate(s^{-1})	0.0001	0.01	1	100	1000
R	0.9883	0.9609	0.9882	0.9879	0.9838
AARE(%)	2.8797	3.2394	4.0213	3.6820	3.8860

3.3 Johnson-Cook damage and fracture model

In order to accurately predict the damage behaviour of air-conditioner fins during forming, it is necessary to test the damage fracture properties of 8011 aluminium alloy.The Johnson-Cook damage model, which is proposed for macroscopic metal damage and which integrates the effects of strain, strain rate and temperature, has been shown to be stable and effective in simulating metal deformation processes[28-30]. Therefore, in this paper, the Johnson-Cook damage fracture model is chosen as the criterion for metal damage fracture, which is expressed as:

$$\varepsilon_f = [N_1 + N_2 \exp(N_3 \sigma^*)](1 + N_4 \ln \dot{\varepsilon}_d^*)(1 + N_5 T^*) \tag{30}$$

Where, ε_f is the fracture strain at the current stress state, temperature, and strain rate. The stress triaxiality is $\sigma^* = \sigma_m/\sigma_{\mathrm{eq}}$, where σ_{eq} is the equivalent stress and $\sigma_m = (\sigma_1 + \sigma_2 + \sigma_3)/3$ is the mean stress; σ_1, σ_2, and σ_3 are the principal stresses. The parameters N_1, N_2, and N_3 describe the effect of stress triaxiality, while N_4 and N_5

describe the strain-rate and temperature effects, respectively. For the damage model, $\dot{\varepsilon}_d^* = \dot{\varepsilon}/\dot{\varepsilon}_{0,d}$, with $\dot{\varepsilon}_{0,d} = 10^{-2}s^{-1}$.

The Johnson-Cook damage fracture model is a function of stress triaxiality, so tensile specimens with different stress triaxiality were designed to determine the fracture strain under different loading paths. The tensile specimens involved in this paper are 0° tensile shear specimen, 45° tensile shear specimen, single notched tensile specimen, and double notched tensile specimen, corresponding to stress triaxiality of 0, 0.197, 0.395, and 0.515, respectively, and the strain at the time of fracture damage of the specimen is taken as the rupture strain in the single notched, double notched, and uniaxial tensile tests.The rupture strains for the three specimens can be adopted equation proposed by Gambirasio et al[31] for calculation. Assuming that the plastic volume of the metallic material remains constant before and after the tensile test, the strain at fracture of the specimens is calculated by measuring the magnitude of the cross-sectional area of the specimens before and after the test, which is given by the formula:

$$\varepsilon_f = \ln(\frac{S_0}{S_1}) \tag{31}$$

Where S_0 is the cross-sectional area of the initial specimen marking section, S_1 is the minimum cross-sectional area at the specimen break, $S_0=dt$, d is the width of the specimen marking section, and t is the specimen thickness. For notched tensile specimens, d is the distance between the two semicircular vertices.

Tensile tests were conducted at room temperature under strain rate $10^{-2}s^{-1}$ loading conditions. Eq. (30) can be simplified as,

$$\varepsilon_f = N_1 + N_2\exp(N_3\sigma^*) \tag{32}$$

Measurements of d and t at initial and fracture of single-notched, double-notched, and uniaxial tensile specimens were carried out using vernier calipers and a spiral micrometer, as shown in Table 5. Substituting into Eq. (31) the corresponding fracture strains ε_{f1}=0.2155, ε_{f2}=0.1828, ε_{f3}=0.2440 can be calculated. Fig. 9 shows the force-displacement curves of 0° and 45° shear tensile specimens of 8011-O aluminium alloy, with maximum displacements of 2.55 mm and 1.66 mm, respectively, corresponding to fracture strains of ε_{f4}=0.3693 and ε_{f5}=0.2830.

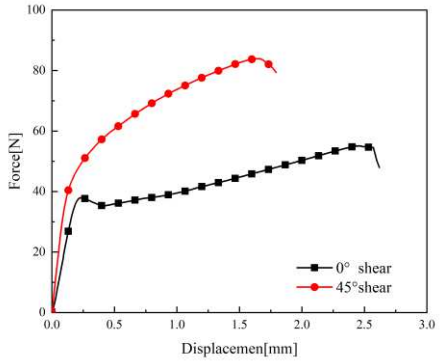


Fig. 9 0° and 45° shear tensile force-displacement curves for 8011 aluminium alloy.

Table 5 The initial and fracture *d* and *t* values of the specimen under $10^{-2}s^{-1}$

		Single notched	Double notched	Uniaxial tensile
Initial	*d*	3.07	4.22	4.85
	t	0.305	0.312	0.318
Fracture	*d*	2.96	4.16	4.56
	t	0.254	0.263	0.265

Based on the fracture strains obtained from the above tests, Origin was used to plot the stress triaxiality versus fracture strain and fit it to the exponential function in Eq. (32), as shown in Fig. 10(a), yielding N_1=-0.0933, N_2=0.4620, and N_3=-0.9968. In order to determine the parameter N_4, dynamic uniaxial tensile tests were conducted at room temperature for the strain rates of $1s^{-1}$, 10^2s^{-1}, and 10^3s^{-1}. Eq. (30) can be simplified as:

$$\varepsilon_f = [-0.0933 + 0.4620\exp(-0.9968\sigma^*)](1 + N_4 \ln\dot{\varepsilon}_d^*) \tag{33}$$

The initial and fracture d and t values of uniaxial tensile specimens at strain rates of $1s^{-1}$, 10^2s^{-1}, and 10^3s^{-1} are given in Table 6, and the corresponding fracture strains were calculated as ε_{f6}=0.2903, ε_{f7}=0.3456, and ε_{f8}=0.3690.

The parameter N_4 was determined by fitting Eq. (33) to the fracture strains from the dynamic uniaxial tensile tests at $\sigma^* = 1/3$. The fit shown in Fig. 10(b) gives $N_4 = 0.0481$.

Table 6 The initial and fracture *d* and *t* values of uniaxial tensile specimens at different strain rates

		$1s^{-1}$	10^2s^{-1}	10^3s^{-1}
Initial	*d*	4.92	4.88	5.02
	t	0.313	0.311	0.315
Fracture	*d*	4.63	4.42	4.55
	t	0.255	0.242	0.242

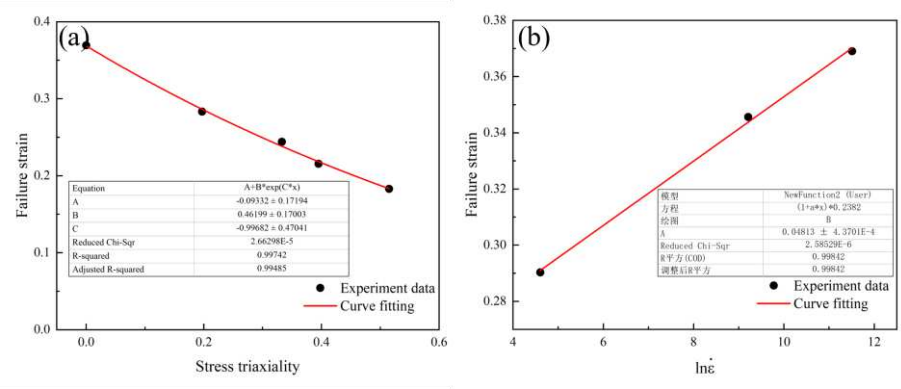


Fig. 10 Johnson-Cook damage model parameter fits: (a) Stress triaxiality-breaking strain curve; (b) strain rate versus fracture strain curve.

4 Numerical simulation of fin forming properties

In order to better understand the forming properties of 8011 aluminium alloy thin plate, numerical simulation of the punching and flanging process of fins is carried out using finite element software. In this section, the deformation characteristics, thinning and damage evolution mechanism of 8011 aluminium alloy during the forming process are analysed.

4.1 Simulation modeling

In this paper, the prefabricated plate obtained from 8011 aluminium alloy rolled plate with the size of Φ40×0.3mm after seven passes of thinning and deep drawing is taken as the research object of numerical simulation, and the deformation of the first seven passes is retained by the predefined field. The mould movement speed was set to 10 mm/min according to the actual production, and the fin forming process was shown in Fig. 11. The parameters of Hill48 yield criterion, Johnson-Cook constitutive model and damage fracture model established above were assigned to the 8011 aluminium alloy preform model, and the mesh division of the preform model was carried out by using shell cells with the mesh size of 0.2mm×0.2mm and the number of meshes of 4762.The coefficient of sliding friction between the preform and the die was set to 0.3.

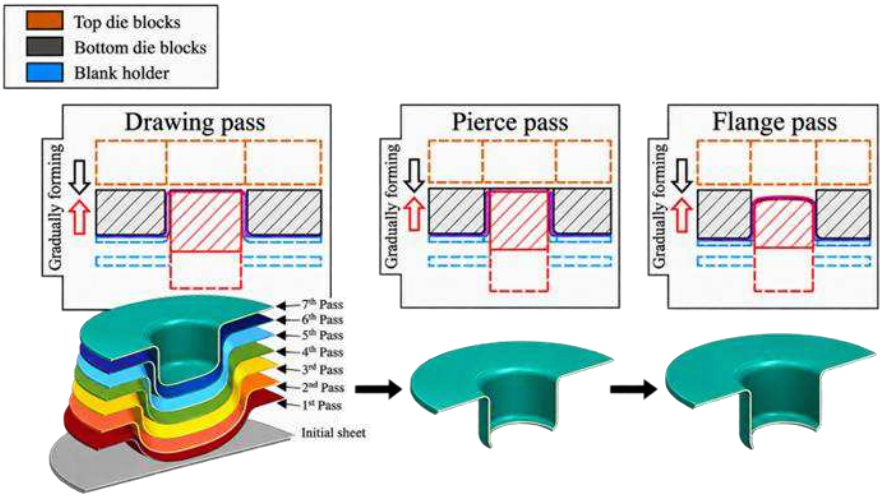


Fig. 11 Schematic diagram of forming process

4.2 Distribution and evolution of wall thickness

Fig. 12 shows the cloud diagram of wall thickness distribution during piercing and flanging forming of 8011-O aluminium alloy fins. It can be seen that material thinning occurs in the rounded area of the punch die, decreasing from 0.3 mm to 0.173 mm in the initial sheet, and thickening occurs in some of the barrel wall areas. This is due to the fact that during the movement of the punch die, an stamping force is exerted on the material at the bottom of the fin, and the material flows plastically under the stamping force, which causes the material in the flange area to flow to the barrel wall area resulting in an increase in the thickness of the barrel wall, and the loss of material caused by the piercing process results in a serious thinning in the rounded corner area of the punch die. In addition, anisotropy also affects the thickness distribution of the material during the forming process, with the thickness of the material being less in the direction along and perpendicular to the rolling direction than in the other directions. This is the same as the result of equivalent force distribution, the fastest flow rate of material along the rolling direction and perpendicular to the rolling direction, resulting in these two directions are less likely to be aggregated, as shown in Fig. 13.

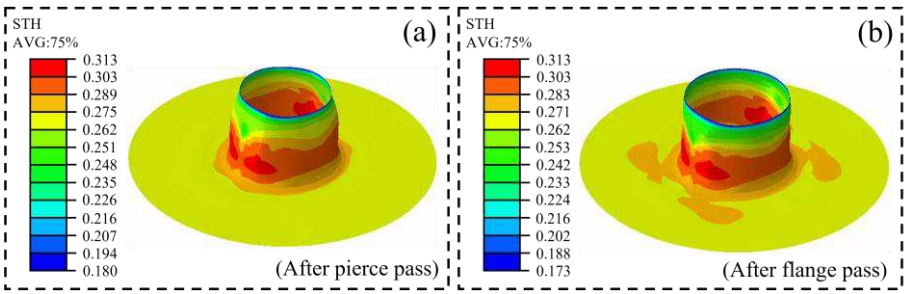


Fig. 12 Distribution of wall thickness after piercing and flanging : (a) piercing forming ; (b) Flanging forming

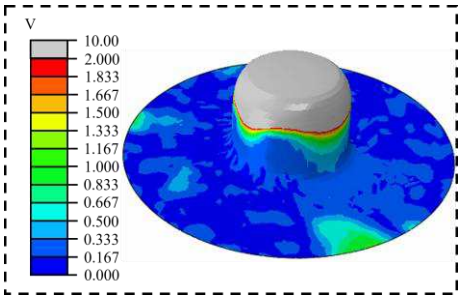


Fig. 13 Material flow rate diagram of piercing process

4.3 Damage evolution

Fig. 14 gives the deformation of the piercing punch die impacting the 8011-O aluminium alloy plate at different moments with an initial velocity of 10 mm/s. When the piercing punch die comes into contact with the 8011-O plate, the piercing punch die intrudes into the plate and damage occurs in the rounded area of the punch die. As the piercing die continues to penetrate the plate, a high stress zone is formed in the material around the edge of the piercing die, and significant plastic deformation and fracture occur in the material in the region of the rounded corner of the die, resulting in a large number of missing finite element meshes. The plate equivalent force peaks when the piercing die just touches the plate, and then the equivalent force gradually decreases. This is due to the conversion of the kinetic energy of the piercing punch into the plastic deformation energy of the plate, the ductile expansion energy of the plate and the thermal energy of the system, as shown in Fig. 15(a). Both plastic deformation and ductile fracture generate heat during piercing, so the thermal energy grows the most and lasts the longest. The ductile fracture of the plate is due to the plastic deformation of the plate and therefore the plastic deformation energy is greater than the ductile fracture energy.

The damage failure mechanism of 8011-O aluminium alloy plate piercing should take into account the dimensional stiffness gradient (SDEG) of the material in addition to the energy change of the system, as can be seen from Fig. 15(b), the value of the SDEG is in the range of 0 to 1, and the higher the value, the more serious the damage of the part is indicated. When the SDEG value is equal to 1, the mesh is deleted. The sporadic red areas in the figure indicate that SDEG is almost equal to 1, reaching the threshold for being deleted.

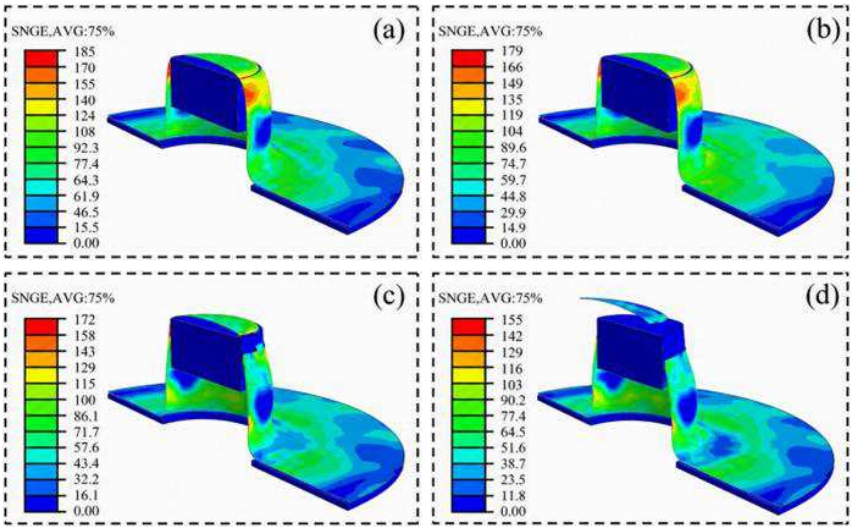


Fig. 14 Deformation of punch stamping plate at different moments : (a) 3.045s ; (b) 3.12s ; (c) 3.195s ; (d) 3.27s

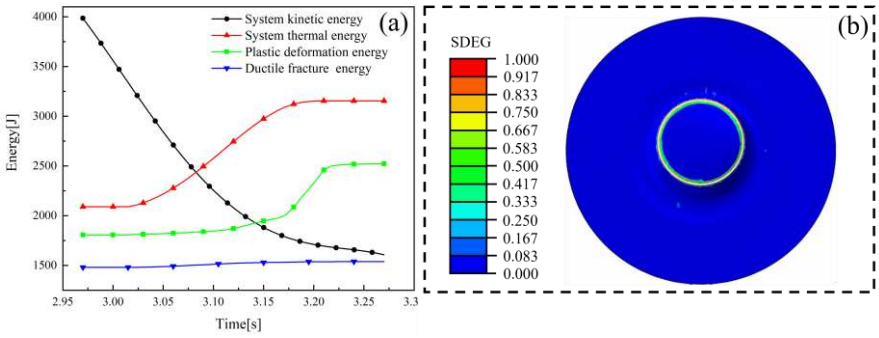


Fig. 15 System energy change and distribution diagram of SDEG : (a) System energy change diagram ; (b) distribution of SDEG

4.4 Reliability verification of process experiments

In order to verify the accuracy of the 8011-O aluminium alloy mechanical model established in this paper in predicting the wall thickness variation and damage fracture location during multi-pass stamping of fins, multi-pass stamping and forming tests of fins were carried out under the same process parameters as those of the finite element model. The wall thickness distribution was measured on the press-formed workpiece at the locations shown in Fig. 16(a). The distribution of the thinning rate between the actual formed workpiece and the simulated formed workpiece is shown in Fig. 16(b). It is easy to see that the relative error of the thinning rate between the actual forming workpiece and the simulated forming workpiece is small, and the maximum relative error is 9.68%. In addition, considering the impact of stamping speed on productivity, this paper also investigates the impact of stamping speed on the forming quality of fins, and carries out finite element simulation analyses and process tests under the condition of stamping speed of 500 mm/s (strain rate of 10^2 s^{-1}). It was found that too high stamping speed would lead to material fracture in

the stamping process, which was also verified by the finite element simulation results, as shown in Fig. 17. In this sense, the 8011-O aluminium alloy mechanical model established above can effectively predict the wall thickness change and damage fracture during the forming process of 8011-O aluminium fins.

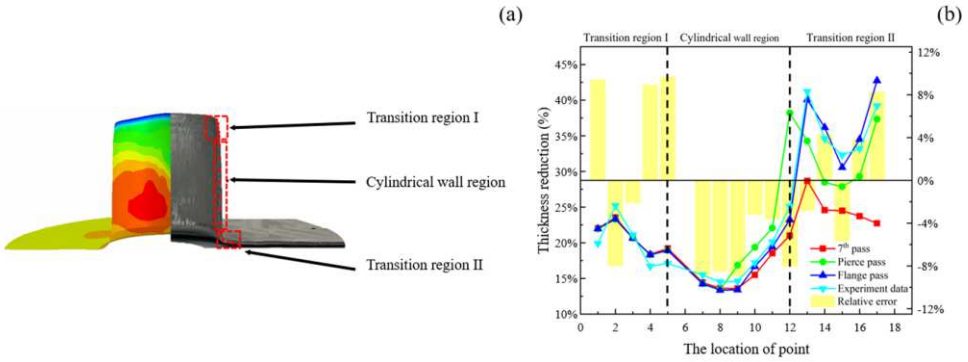


Fig. 16 The change of wall thickness thinning/thickening rate with the forming passes : (a) the position of the point ; (b) wall thickness distribution

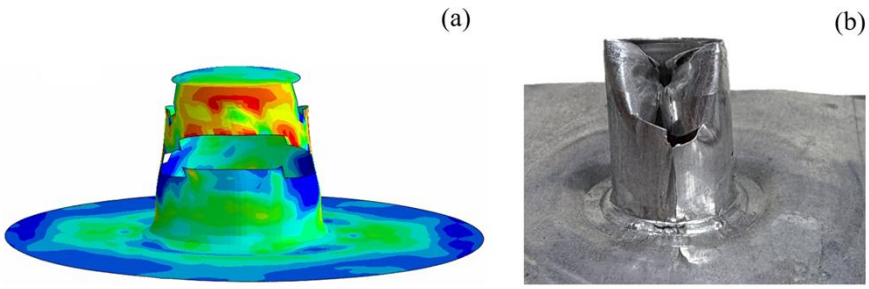


Fig. 17 Simulation verification diagram and process test diagram : (a) Simulation verification diagram ; (b) Process experimental diagram

5 Conclusions

In order to investigate the mechanical behaviour of 8011-O aluminium alloy during the stamping of air-conditioner radiator fins, uniaxial loading tests with different orientations and strain rates, as well as fracture performance tests with different stress states were carried out. Based on the mechanical property data obtained from the tests, the anisotropic yield criterion, dynamic constitutive model and damage fracture model of 8011-O aluminium alloy were established. Numerical simulation of the press forming of air-conditioner radiator fins was carried out. The fracture location during fin forming is predicted by thickness distribution and damage evolution, which is of great significance to improve the material utilization of 8011-O aluminium alloy during press forming and optimize the fin forming parameters. The conclusions are as follows:

(1) Based on the uniaxial tensile test data in different directions, the stress principal axis direction is introduced, and the parameters of the original Hill48 yield model are extended, so that

the modified Hill48 yield model is proposed and the process of determining the model parameters is given. The modified Hill48 model can accurately predict the uniaxial tensile yield stress and r-value at the same time, and can reflect the changes of yield stress and *r*-value with angle.

(2) The prediction ability of the modified Johnson-Cook principal model was improved, and its maximum average relative error (*AARE*) was only 4.0213%. The fracture performance tests of 8011-O aluminium alloy under different stress states were carried out, the fracture strains corresponding to different stress states were obtained, and the Johnson-Cook damage fracture model applicable to 8011-aluminium alloy thin plate was established.

(3) A finite element model of the fin stamping process was developed and the material mechanics model was applied to the fracture prediction of fins. The maximum relative error between the actual formed workpiece and the simulated formed workpiece thinning rate is 9.68%. And too high stamping speed will lead to material fracture in the stamping process.

References

[1] Ma L, Li Y, Wang J, et al. Numerical investigation of deformation and residual stress in vacuum brazing of titanium alloy plate-fin structure[J]. Vacuum, 2024, 227: 113443.

[2] Hou J, Deng P, Wang S, et al. Study on formability and microstructure evolution of hot deep drawing manufactured 7005 aluminum alloy sheet metal[J]. Materials Today Communications, 2023, 36: 106794.

[3] Wang J, Ling X, Zhang W, et al. Microstructures and mechanical properties of friction stir welded butt joints of 3003-H112 aluminum alloy to 304 stainless steel used in plate-fin heat exchanger[J]. Journal of Materials Research and Technology, 2022, 21: 3086-3097.

[4] Hu X, Li Y, Liu Y, et al. Simulation, experiment and application of the damage analysis in the sheet plate forming based on modified Lemaitre model[J]. Materials Today Communications, 2024, 40: 109715.

[5] Zhang Y, Duan Y, Fu P, et al. Constitutive modeling based on non-associated flow rule for anisotropic sheet metals forming[J]. Materials Today Communications, 2023: 107086.

[6] Zhang X, Cai Z Y, Gao J X, et al. Face sheet defects in plastic forming of aluminum foam sandwich panel: theoretical models, numerical and experimental studies[J]. Journal of Materials Research and Technology, 2023, 26: 4351-4364.

[7] Mu Z, Wang W, Zhang S, et al. Towards improved description of plastic anisotropy in sheet metals under biaxial loading: A novel generalization of Hill48 yield criterion[J]. Materials Today Communications, 2024, 41: 110222.

[8] SHANG H, WANG S, LOU Y. Modeling and characterization on electroplastic effect during dynamic deformation of 5182-O aluminum alloy[J]. Transactions of Nonferrous Metals Society of

China, 2024, 34(8): 2455-2475.
[9] Cui J, Chen L, Li Y, et al. Effects of annealing treatment on mechanical properties of 8011 aluminum alloy after cryogenic rolling[J]. Metallurgical Research & Technology, 2019, 116(2): 219.
[10] Jiang X, Li N, He H, et al. Effect of cryogenic treatment on mechanical properties and microstructures of 3102 Al-alloy[C]//Materials Science Forum. Trans Tech Publications Ltd, 2007, 546: 845-848.
[11] Jung S H, Bae G, Kim M, et al. Effect of natural aging time on anisotropic plasticity and fracture limit of Al7075 alloy[J]. Materials Today Communications, 2022, 31: 103553.
[12] Mu Z, Zhao J, Meng Q, et al. Limitation analysis of the Hill48 yield model and establishment of its modified model for planar plastic anisotropy[J]. Journal of Materials Processing Technology, 2022, 299: 117380.
[13] Liu H, Jin T, Qiu J, et al. Anisotropic constitutive modeling with the considerations of two strategies in describing the distorted hardening of AA6061 under tension-dominated loading conditions[J]. Journal of Materials Research and Technology, 2024, 29: 571-588.
[14] Wu H, Zhuang X, Zhang W, et al. Anisotropic ductile fracture: Experiments, modeling, and numerical simulations[J]. Journal of Materials Research and Technology, 2022, 20: 833-856.
[15] Wu B, Wang Y, Liu X, et al. Investigation on dynamic deformation behavior of 7A75 aluminum alloy over wide strain rates and constitutive model establishment[J]. Journal of Materials Research and Technology, 2024, 30: 5963-5976.
[16] Rudnytskyj A, Simon P, Jech M, et al. Constitutive modelling of the 6061 aluminium alloy under hot rolling conditions and large strain ranges[J]. Materials & Design, 2020, 190: 108568.
[17] Wan J, Zhu Y, Zhang Y, et al. Strain rate effect and dynamic constitutive model of 7A04-T6 high-strength aluminium alloy[C]//Structures. Elsevier, 2023, 53: 1250-1266.
[18] Shen W, Xue F, Li C, et al. Study on constitutive relationship of 6061 aluminum alloy based on Johnson-Cook model[J]. Materials Today Communications, 2023, 37: 106982.
[19] Jia Z, Guan B, Zang Y, et al. MJ-C model of aluminum alloy 6016-T6 sheets at low dynamic strain rates[J]. Materials Science and Engineering: A, 2021, 820: 141565.
[20] Chang L, Yuan S, Huang X, et al. Determination of Johnson-Cook damage model for 7xxx laminated aluminum alloy and simulation application[J]. Materials Today Communications, 2023, 34: 105224.
[21] Bharti S, Gupta A, Krishnaswamy H, et al. Evaluation of uncoupled ductile damage models for fracture prediction in incremental sheet metal forming[J]. CIRP Journal of Manufacturing Science and Technology, 2022, 37: 499-517.
[22] Guo Y, Xie Y, Wang D, et al. An improved damage-coupled viscoplastic model for predicting

ductile fracture in aluminum alloy at high temperatures[J]. Journal of Materials Processing Technology, 2021, 296: 117229.

[23] Hou W, Liu Z, Shi J, et al. On the mechanical performance and damage evolution of rivet-bonded composite T-joint under three-point bending: A combined experimental and numerical study[J]. Thin-Walled Structures, 2023, 186: 110668.

[24] Hill R, Hutchinson J W. Differential hardening in sheet metal under biaxial loading: a theoretical framework[J]. 1992.

[25] Öztekin E, Pul S, Hüsem M. Experimental determination of Drucker-Prager yield criterion parameters for normal and high strength concretes under triaxial compression[J]. Construction and Building Materials, 2016, 112: 725-732.

[26] Stoughton T B. A non-associated flow rule for sheet metal forming[J]. International Journal of Plasticity, 2002, 18(5-6): 687-714.

[27] Li P, Yu R, Yan S, et al. Study on deformation behavior of Ti60 alloy based on multi-physics coupling[J]. Materials Today Communications, 2024, 38: 107931.

[28] Lai X, Li H, Li C, et al. Modelling and analysis of micro scale milling considering size effect, micro cutter edge radius and minimum chip thickness[J]. International Journal of Machine Tools and Manufacture, 2008, 48(1): 1-14.

[29] Wang Z, Zhang H, Li Z, et al. Crystal plasticity finite element simulation and experiment investigation of nanoscratching of single crystalline copper[J]. Wear, 2019, 430: 100-107.

[30] Guo X, Sun X, Tian X, et al. Simulation of ballistic performance of a two-layered structure of nanostructured metal and ceramic[J]. Composite Structures, 2016, 157: 163-173.

[31] Zhang Z, Wu Y, Huang F. Effect of stress triaxiality cut-off value in the fracture criterion on predicting the ballistic behavior of Al2024-T351 plate impacted by blunt-hemisphere-and ogival-nosed projectiles[J]. Journal of Materials Research and Technology, 2023, 25: 138-165.